Theoretical Investigation of Air Breakdown Direct Current Triboelectric Nanogenerator

Sixing Xu[1,2], Hengyu Guo[2,3], Steven L. Zhang[2], Long Jin[2], Wenbo Ding[4], Xiaohong Wang[1] & Zhong Lin Wang[2,3]

[1]Department of Microelectronics and Nanoelectronics, Tsinghua University, Beijing 100084, China.[2]School of Materials Science and Engineering, Georgia Institute of Technology, Atlanta, GA 30332-0245, USA. [3]Beijing Institute of Nanoenergy and Nanosystems, Chinese Academy of Sciences, Beijing 100083, China. [4]Tsinghua-Berkeley Shenzhen Institute, Tsinghua Shenzhen International Graduate School, Tsinghua University, Shenzhen 518055, China. Correspondence and requests for materials should be addressed to X. W. (email: wxh-ime@tsinghua.edu.cn) or to Z.L.W. (email: zhong.wang@mse.gatech.edu)

Abstract

Triboelectric nanogenerator (TENG), which harvests ubiquitous ambient mechanical energy, is a promising power source for the distributed energy. Recently reported new generation direct current TENG (DC-TENG) based on the air breakdown effect has exhibited unique advantages over conventional modes of TENG devices, such as free-of-rectification and intrinsic switching behavior. However, owing to different working mechanisms and output characteristics, the existing theory and power management strategies are not suitable for in-depth understanding and further advancement of air breakdown DC-TENG. Herein, a theoretical study and experimental verification that systematically investigate the physics, output characteristics and the power management strategy of air breakdown DC-TENG is presented. A general simulation model is then proposed and verified through a statistical analysis method. Contrary to previous understanding of highly conductive breakdown pathway, a huge resistance is observed and causes inevitable energy loss, which is regarded to be caused by corona discharge. Finally, device optimization and power management strategies are discussed, and a fundamental guidance is given for rational design of air breakdown DC-TENG.

Triboelectric nanogenerator (TENG), as a mechanical energy harvester, has been proven to be a promising power alternative for distributed energy due to the features of high power, environmentally friendly and easy-scalable[1-9]. Over the past few years, TENG devices has been quickly developed and widely applied in numerous applications, including energy harvesting, high-voltage power source, active sensing, human machine interface and etc[10-16]. Accompanied with the development of TENG, the physical mechanism, simulation model and power management strategy have also been proposed and verified by researchers[17-27]. These theories serve as effective guidelines and have boosted the advancement of the field. However, it is found that the power efficiency of current TENG devices has hit the wall due to two practical problems: firstly, current TENG devices are easily associated with uncontrolled electrostatic breakdown due to their ultrahigh voltage, so that the generated charge cannot be held and released at the highest voltage[28-31]; secondly, the output of these TENG devices are featured by alternating current and high matching impedance, which bring inevitable energy loss during the energy conversion process[32, 33].

Recently, a new generation of TENG based on contact electrification and air breakdown effect has been developed and show great advantage toward conventional modes of TENG[34-37]. The breakdown process is “one way”, which causes a direct current output, making the rectification module to be unnecessary. In addition, different from previous four modes of TENG, the charges of the air breakdown direct current TENG (DC-TENG) are released with the breakdown potential during the discharge so that energy efficiency can be naturally higher than those being released instantaneously. Some experimental pioneering works have shown the outstanding performances of air breakdown DC-TENG[34-36]. However, the systematic operation mechanism and optimization path have not been investigated yet, which ascribed to the different physics effects and unfeasibility of conventional theories for the air breakdown DC-TENG.

Herein, through both simulation and experiment verification, we report a theoretical research and simulation model for the air breakdown DC-TENG. To overcome the randomness of the breakdown peaks, an automatic statistical analysis and fitting method is proposed and serve as an effective tool in investigating the theory of the air breakdown DC-TENG. Based on the proposed method, an equivalent circuit of air breakdown DC-TENG is derived, containing a current source, an inner capacitor, a diode, a voltage-controlled gate. Moreover, different from the conventional cognition, which believes that breakdown path should be highly conductive, a large resistance is observed in this circuit model, which causes inevitable energy loss and a slow discharge process. Based on the theoretical model, the power management strategy for such circuit model is investigated, suggesting a potential of up to 100% of power efficiency. Finally, the key challenge and future optimization direction are discussed.

Recently, several different air breakdown DC-TENG structures have been reported and they are both caused by contact electrification and air discharge effect, which is the basic difference with conventional TENG devices[34-37]. Similar to the unified simulation model of conventional TENGs[38], which greatly facilitate its optimization, a unified model of air breakdown DC-TENG is also need to be developed for the further advancement, standardization and industrialization. One of the most exemplary air breakdown DC-TENG structure[36], as illustrated in Figure 1a, is utilized to investigate the theory of air breakdown DC-TENG. When the bottom electrode slides on the dielectric layer, opposite triboelectric charges will be generated due to the contact electrification and then the generated negative charge on the dielectric would induce positive charges on the sharp top electrode[7, 8]. According to Gauss theorem, the electric field strength near the top electrode can easily exceed the limit of air breakdown, causing ionization of air molecules. Detached electrons will be accelerated by the electric filed and collides with more air molecules. As studied in breakdown theory[39], three stages can be roughly divided with the increasing of accumulated charges, as shown in Fig. 1b: 1) turn-off state: the electric field strength is too small for ionization and little current can be transmitted by the near-insulated air; 2) corona discharge state: the electric field strength can ionize air molecule but not enough for breakdown. In this stage, the ionization and recombination rates are competing and reach a balance at a certain distance from the top electrode. From the circuit aspect, a continuous current will be provided with the movement of the slides, and the current-voltage can be approximated as Townsend relation:

$$I = AU(U - U_C) \quad (1)$$

where A is a structure and environment related constant, U is the voltage between top and bottom electrodes and U_C is the critical voltage for corona discharge; 3) breakdown state: the electric field strength is strong enough to cause an electron avalanche and a conductive pathway between top electrode and dielectric layer will be established.

According to above analysis, a simulation circuit model, as shown in Fig. 1c, was proposed. Firstly, a current source and an inner capacitor are proposed to demonstrate the effect of sliding triboelectrification, while a diode is added to describe the 'one-way' characteristic of discharge process. Afterward, a voltage-controlled resistor is proposed, representing the variable path resistance during different states. When little charge is accumulated on the top electrode, which is denoted as period one (P1), the gas between top electrode and tribo-layer is unionized, making it behave similar to an insulator, making the resistance extremely large. While the voltage exceeds the ionization critical voltage[40], denoted as period two (P2), corona current appears and greatly decreases the resistance[39]. Furtherly, in the period three (P3), the voltage between top electrode and bottom electrode exceeds the breakdown limitation and the resistance sharply decreases to near zero, representing the short-circuit of the breakdown path. The states of the switching system with controlling voltage can be expressed by Eqs. (2).

$$\text{States} = \begin{cases} P1:\ R \to \infty;\ Switch = off & (U < U_C) \\ P2:\ R = \frac{A}{U - U_C};\ Switch = off & (U_C < U < U_{Break}) \\ P3:\ R \to 0;\ Switch = on & (U > U_{Break}) \end{cases} \quad (2)$$

where U_{Break} is the critical electron avalanche voltage which can be predicted by Paschen's Law. It should be mentioned that, different from previous thoughts which simply believe the discharge should only be caused by breakdown, we insist that a corona discharge process is inevitable. This corona discharge is significant to current air breakdown DC-TENG, because the released charge in this process is comparable to the triboelectric charge.

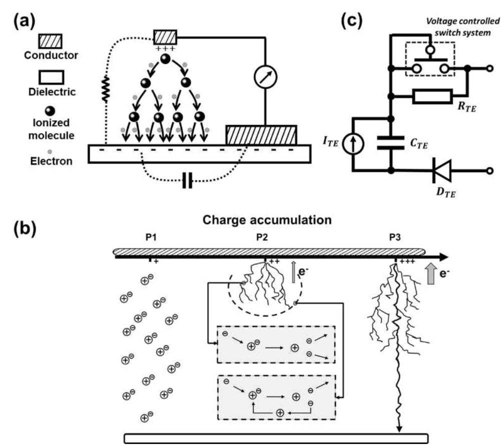

Figure 1. The operation mechanism and simulation model of air breakdown DC-TENG. (a) The concept illustration of basic air breakdown DC-TENG device and operation mechanism. **(b)** The discharge process with three stages. **(c)** The simulation circuit model of the air breakdown DC-TENG.

For the investigation of a circuit black box with multiple parameters, testing the output under given inputs and loads and then do the fitting, is the most effective and reliable method. A typical short-circuit current output of the air breakdown DC-TENG is shown in Fig. 2a (see *Method* for device fabrication and testing). It can be observed that the discharge peaks do not have a fixed magnitude and time interval, but randomly distributed around the mean value, which is resulted from the randomness of the collision of ions. Therefore, it is not rigorous to verify the simulation model through single discharge process, instead statistic method with sufficient data should be used to get convincing results. The detailed structure of the peak is demonstrated in Fig. 2(b) (c). As each discharge peak is caused by capacitive charge/discharge process, the current/voltage should obey the form of negative exponential, as listed in Eqs. (3), and the half-life period should be written as Eqs. (4).

$$V = V_0 e^{-\frac{t}{RC}} = V_0 e^{-\frac{t}{(R_{TE}+R_{EX})C_{TE}}} \quad (3)$$

$$T_{half} = \ln(2)\, C_{TE} R_{TE} + \ln(2)\, C_{TE} R_{EX} \quad (4)$$

where V_0 is the initial voltage, R_{TE} and C_{TE} are the intrinsic resistance and capacitance, R_{EX} is the external load resistance and T_{half} is the half-life period. An automatic program for peak acquisition and analysis was developed, of which the algorithm is shown in Supplementary Scheme 1 (code is available in Supplementary *Code 1*). Specifically, each peak can be detected automatically by comparing the data point with data before and after, with a minimum peak width and height thresholds. After that, the half-life period is obtained by traverse all data points and select the closest one. As the time constants of a capacitive charge/discharge circuit is proportional to the resistance, a systematic test was done to investigate different external resistance and its relationship with the peak's half-life periods. The current output with load resistances of 100M Ω and 10G Ω are shown in Fig. 2(d)(e), with the detailed peak shapes insets. It is clear that the half-life periods obviously increase with the increase of external resistance. Interestingly, with the external resistance of 10G Ω, the current did not drop to zero for each peak due to a slow discharge process, but it contributes a stable base current, which can be a solution for stable DC output[33]. The analysis of the time constants with the three representative external resistances (short-circuit, 100M Ω and 10G Ω) is shown in Fig. 2f, showing the mean time constants of 2.3 ms, 4.5 ms and 134.8 ms, respectively. In addition, the standard deviations of those time constants are only 0.36 ms, 0.71 ms and 14.7 ms, demonstrating the high reliability and repeatability of the calculated time constants.

The fitting of the time constants with different external resistances is shown in Fig. 2g. As expected, the fitting curve demonstrates a correlation coefficient as high as 0.997, which strongly validates the capacitive discharge hypothesis. Accordingly, the intrinsic capacitance and resistance are calculated to be 21.812 pF and 157.75 MΩ, respectively. The magnitude of capacitance is in accordance to the expectation; however, the resistance is much larger than it should be for a breakdown conductive path, which generally below 10 Ω for the millimeter-level distance. It is reasonable to believe that the corona discharge plays an important role during the discharge process. The transferred charge with operation periods is shown in Fig. 2h, in which the charge transferred in operation cycles is kept almost constant, indicating the high stability with sufficient amount of random discharge peaks. Moreover, with the increase of the move speed, i.e. increase of the operation frequency, the transferred charge decreases, which should be ascribed to the time interval is too short for the release of the charge.

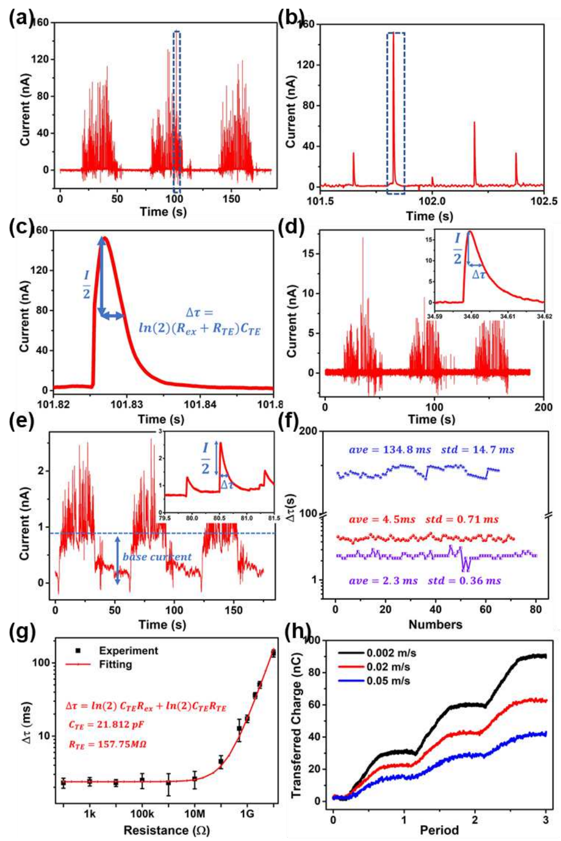

Figure 2. The outputs analysis of air breakdown DC-TENG. (a) Short-circuit current output of air breakdown DC-TENG. **(b)(c)** Detailed curve shape of the discharge peak, with **(c)** the half-life period detecting and fitting method. **(d)** The current output with load resistance of 100M Ω. **(e)** The current output with load resistance of 10G Ω. **(f)** The mean value and standard deviation of half-life periods with load resistances of 0 Ω(purple), 100M Ω(red) and 10G Ω(blue). **(g)** The fitting of half-life periods with different external resistances. **(h)** The transferred charges with different slider moving speed (moving distance is fixed by 6 cm). All the tests in (a)-(g) are carried out with period of 60s.

Switch-mode power techniques are the most widely used DC-DC conversion methods in power management circuits and have also been successfully applied to boost the performance of TENG devices[41,42]. However, introducing an external electronic switch for TENG is difficult due to the limitation of the threshold voltage and channel capacitance of electronic switches. Also, mechanical switch generally exhibits long response time, causing non-ideal discharge during the switching process. Another issue is that it is difficult to detect whether the voltage output is at the peak through electronic switch, which is the key for the power management strategy. Therefore, the air breakdown DC-TENG with naturally switching feature is promising to reduce the complexity of power management circuit and perform high power efficiency. Nevertheless, due to the intrinsic resistance brought by the discharge process, current air breakdown DC-TENG devices do not show the potential benefit. The power output with various load resistances is shown in Fig. 3a, indicating a matching impedance around 2G Ω, which should be much lower for an ideal switching system. In addition, the simulation of the power output for each discharge process with the parameters listed in Supplementary Table. 1 and time interval of 0/10/20/50 ms is shown. The experiment results are well fitted with the circuit simulation with 20 ms intervals between each discharge process, which strongly proves the simulation model again.

Even though considerable resistance exists in current air breakdown DC-TENG, there is still a significant advantage for power management. The basic idea of utilizing the switching feature of the air breakdown DC-TENG for power management is illustrated in Fig. 3b. When the peak discharge occurred, the switch is turned on and the charge accumulated flows through the external inductor L_{ex} to the load. In this case the device output is prevented from increasing immediately to its peak value as the inductor stores energy taken from the increasing output. Meanwhile, charge on C_{ex} builds up gradually during the 'on' period. As the accumulated charge been released, the switch is turned off. In this stage, the energy stored in the magnetic field around L_{ex} and in the electric field around C_{ex} are released back to the load. In such, the original pulse output with high voltage can be turned to stable output with applicable voltage level. The efficiency of the proposed power management circuit can be calculated based on the state Eqs. (5):

$$\frac{Q_{TE}}{C_{TE}} + R_{TE}\frac{dQ_{TE}}{dt} + L\frac{d^2Q_{TE}}{dt^2} = V_0 \quad (5)$$

where Q_{TE} is the charge for each release process, R_{TE} and C_{TE} are the intrinsic resistance and capacitance, L is the external inductor and V_0 is the stable voltage of the external capacitor. The energy transferred to the load and the power efficiency can be calculated (see detail in Supplementary Note 1). The power efficiency is defined as:

$$\eta = \frac{E_{TE} - E_R - E_c}{E_{TE}} \quad (6)$$

where E_{TE} is the system energy capacitive energy before discharge, E_c is the system capacitive energy remained after discharge, and E_R is the energy wasted on the inner resistor. Fig. 3c plots the power efficiency versus the quality factor $4L/R^2C$. It can be observed that the efficiency is negatively related with the intrinsic resistance, yet positively related to the external inductance. With the increase of the quality factor, the power efficiency will gradually increase to about 40% with $4L/R^2C$ = 10, and nearly 100% when $4L/R^2C$ >1000. The effectiveness of such power management strategy is furtherly verified through circuit simulation (Supplementary Fig. S2).

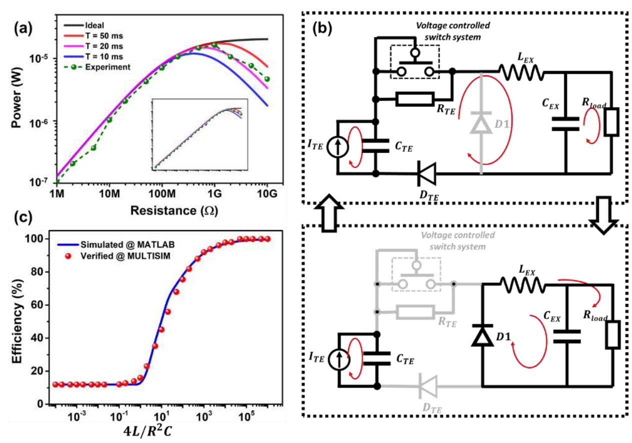

Figure 3. The power output and management strategy for air breakdown DC-TENG. (a) The power out with different external resistances and simulations with different time interval between peaks. **(b)** The proposed circuit scheme for the power management. **(c)** The theoretical power efficiency of the power management circuit and circuit simulation result.

From the above analysis, it is clear to see the resistance caused by corona discharge is the main obstacle for achieving high power efficiency in real applications. Therefore, the main effort should been put into reducing the charge been released through corona discharge, i.e. make the breakdown process been the dominant discharge route. Moreover, the impact of device structure to the simulation model is also investigated through controlled experiments, as shown in Supplementary discussion. In such, several potential strategies can be carried out in the future device development: 1) increase the charge accumulation rate so that the corona discharge process can be shorter. To this end, methods like increasing the surface charge density and mechanical operation speed can be effective; 2) decrease the breakdown avalanche critical voltage. Similarly, this method can also reduce the corona discharge loss. Therefore, adjusting device structure and atmosphere to approach the lowest point according to the Paschen's Law can be the answer; 3) skip the corona discharge process. The most efficient strategy is to accumulate the charge without discharge, until it meets the requirement of breakdown.

In conclusion, we have systematically investigated the operation mechanism of air breakdown DC-TENG and especially pointed out the inevitability of the corona discharge process and related resistance in simulation model. Based on sufficient amount of half-periods time with various external resistances, the capacitive discharge model has been well fitted with a correlation efficient of 0.997, strongly proved the hypothesis of discharge model. Based on the simulation model, the potential power management strategies for air breakdown DC-TENG are discussed, showing that in spite of the intrinsic resistance, high power efficiency could also be obtained with external inductor. At last, we point out the key for future optimization of air breakdown DC-TENG is to reduce the corona discharge and improve the breakdown, so that the power efficiency can be greatly boosted. We believe that after the establishment of the theoretical model, the air breakdown DC-TENG will be greatly boosted and exhibits its huge potential in power sources, active sensing and all related fields.

Supplementary material:

See the supplementary material for the signal analysis algorithm, device fabrication, output measurement, the impact of device structure and the theoretical calculation of power efficiency.

This work was supported by the National Natural Science Foundation of China (Grant No. 61834003, 61531166006), the 973 Program of China (Grant No. 2015CB352106) and the Hightower Chair foundation. S. X. thanks China Scholarship Council for supplying oversea scholarship (201806210286).

Data availability:

The data that support the plots within this paper and other finding of this study are available from the corresponding authors upon reasonable request.

References:

1. F.-R. Fan, Z.-Q. Tian and Z. L. Wang, *Nano energy*, 2012, **1**, 328-334.
2. H. Guo, M.-H. Yeh, Y. Zi, Z. Wen, J. Chen, G. Liu, C. Hu and Z. L. Wang, *ACS nano*, 2017, **11**, 4475-4482.
3. Z. L. Wang, J. Chen and L. Lin, *Energy Environmental Science*, 2015, **8**, 2250-2282.
4. Z. L. Wang, *ACS nano*, 2013, **7**, 9533-9557.
5. Z. L. Wang, *Materials Today*, 2017, **20**, 74-82.
6. Z. L. Wang, *Nano Energy*, 2018, **54**, 477-483.
7. Z. L. Wang, *Nano Energy*, 2020, **68**, 104272.
8. C. Xu, Y. Zi, A. C. Wang, H. Zou, Y. Dai, X. He, P. Wang, Y. C. Wang, P. Feng and D. Li, *Advanced Materials*, 2018, **30**, 1706790.
9. Z. L. Wang, *Nano Energy*, 2019, **58**, 669-672.
10. J. Wang, S. Li, F. Yi, Y. Zi, J. Lin, X. Wang, Y. Xu and Z. L. Wang, *Nature communications*, 2016, **7**, 1-8.
11. W. Ding, J. Zhou, J. Cheng, Z. Wang, H. Guo, C. Wu, S. Xu, Z. Wu, X. Xie and Z. L. Wang, *Advanced Energy Materials*, 2019, **9**, 1901320.
12. G. Liu, H. Guo, S. Xu, C. Hu and Z. L. Wang, *Advanced Energy Materials*, 2019, **9**, 1900801.
13. L. Jin, B. Zhang, L. Zhang and W. Yang, *Nano Energy*, 2019, 104086.
14. N. Arora, S. L. Zhang, F. Shahmiri, D. Osorio, Y.-C. Wang, M. Gupta, Z. Wang, T. Starner, Z. L. Wang and G. D. Abowd, *Proceedings of the ACM on Interactive, Mobile, Wearable*, 2018, **2**, 1-28.
15. M. Xu, P. Wang, Y. C. Wang, S. L. Zhang, A. C. Wang, C. Zhang, Z. Wang, X. Pan and Z. L. Wang, *Advanced Energy Materials*, 2018, **8**, 1702432.
16. S. L. Zhang, M. Xu, C. Zhang, Y.-C. Wang, H. Zou, X. He, Z. Wang and Z. L. Wang, *Nano Energy*, 2018, **48**, 421-429.
17. S. Niu, Y. Liu, X. Chen, S. Wang, Y. S. Zhou, L. Lin, Y. Xie and Z. L. Wang, *Nano Energy*, 2015, **12**, 760-774.
18. S. Niu, Y. Liu, S. Wang, L. Lin, Y. S. Zhou, Y. Hu and Z. L. Wang, *Advanced materials*, 2013, **25**, 6184-6193.

19. S. Niu, Y. Liu, S. Wang, L. Lin, Y. S. Zhou, Y. Hu and Z. L. Wang, *Advanced Functional Materials*, 2014, **24**, 3332-3340.
20. S. Niu, S. Wang, L. Lin, Y. Liu, Y. S. Zhou, Y. Hu and Z. L. Wang, *Energy Environmental Science*, 2013, **6**, 3576-3583.
21. S. Niu and Z. L. Wang, *Nano Energy*, 2015, **14**, 161-192.
22. Y. Zi, S. Niu, J. Wang, Z. Wen, W. Tang and Z. L. Wang, *Nature communications*, 2015, **6**, 1-8.
23. Y. Zi, J. Wang, S. Wang, S. Li, Z. Wen, H. Guo and Z. L. Wang, *Nature communications*, 2016, **7**, 1-8.
24. S. Wang, L. Lin, Y. Xie, Q. Jing, S. Niu and Z. L. Wang, *Nano letters*, 2013, **13**, 2226-2233.
25. W. Liu, Z. Wang, G. Wang, G. Liu, J. Chen, X. Pu, Y. Xi, X. Wang, H. Guo and C. Hu, *Nature communications*, 2019, **10**, 1-9.
26. J. Peng, S. D. Kang and G. J. Snyder, *Science advances*, 2017, **3**, eaap8576.
27. A. Ghaffarinejad, J. Y. Hasani, R. Hinchet, Y. Lu, H. Zhang, A. Karami, D. Galayko, S.-W. Kim and P. Basset, *Nano Energy*, 2018, **51**, 173-184.
28. J. Fu, X. Xia, G. Xu, X. Li and Y. Zi, *ACS nano*, 2019, **13**, 13257-13263.
29. X. Xia, J. Fu and Y. Zi, *Nature communications*, 2019, **10**, 1-9.
30. J. Wang, C. Wu, Y. Dai, Z. Zhao, A. Wang, T. Zhang and Z. L. Wang, *Nature communications*, 2017, **8**, 1-8.
31. Y. Zi, C. Wu, W. Ding and Z. L. Wang, *Advanced Functional Materials*, 2017, **27**, 1700049.
32. S. Xu, L. Zhang, W. Ding, H. Guo, X. Wang and Z. L. Wang, *Nano Energy*, 2019, **66**, 104165.
33. C. Chen, L. Chen, Z. Wu, H. Guo, W. Yu, Z. Du and Z. L. Wang, *Materials Today*, 2020, **32**, 84-93.
34. G. Cheng, H. Zheng, F. Yang, L. Zhao, M. Zheng, J. Yang, H. Qin, Z. Du and Z. L. Wang, *Nano Energy*, 2018, **44**, 208-216.
35. J. Luo, L. Xu, W. Tang, T. Jiang, F. R. Fan, Y. Pang, L. Chen, Y. Zhang and Z. L. Wang, *Advanced Energy Materials*, 2018, **8**, 1800889.
36. D. Liu, X. Yin, H. Guo, L. Zhou, X. Li, C. Zhang, J. Wang and Z. L. Wang, *Science advances*, 2019, **5**, eaav6437.
37. Y. Yang, H. Zhang and Z. L. Wang, *Advanced Functional Materials*, 2014, **24**, 3745-3750.
38. S. Niu, Y. S. Zhou, S. Wang, Y. Liu, L. Lin, Y. Bando and Z. L. Wang, *Nano Energy*, 2014, **8**, 150-156.
39. Y. Raizer, *Spark discharge*, Routledge, 2017.
40. A. S. Gibson, J. A. Riousset and V. P. J. N. E. R. P. S. A. R. J. Pasko, 2009, **7**, 1-17.
41. S. Xu, W. Ding, H. Guo, X. Wang and Z. L. Wang, *Advanced Energy Materials*, 2019, **9**, 1900772.
42. S. Xu, W. Liu, B. Hu and X. Wang, *Nano Energy*, 2019, **58**, 803-810.

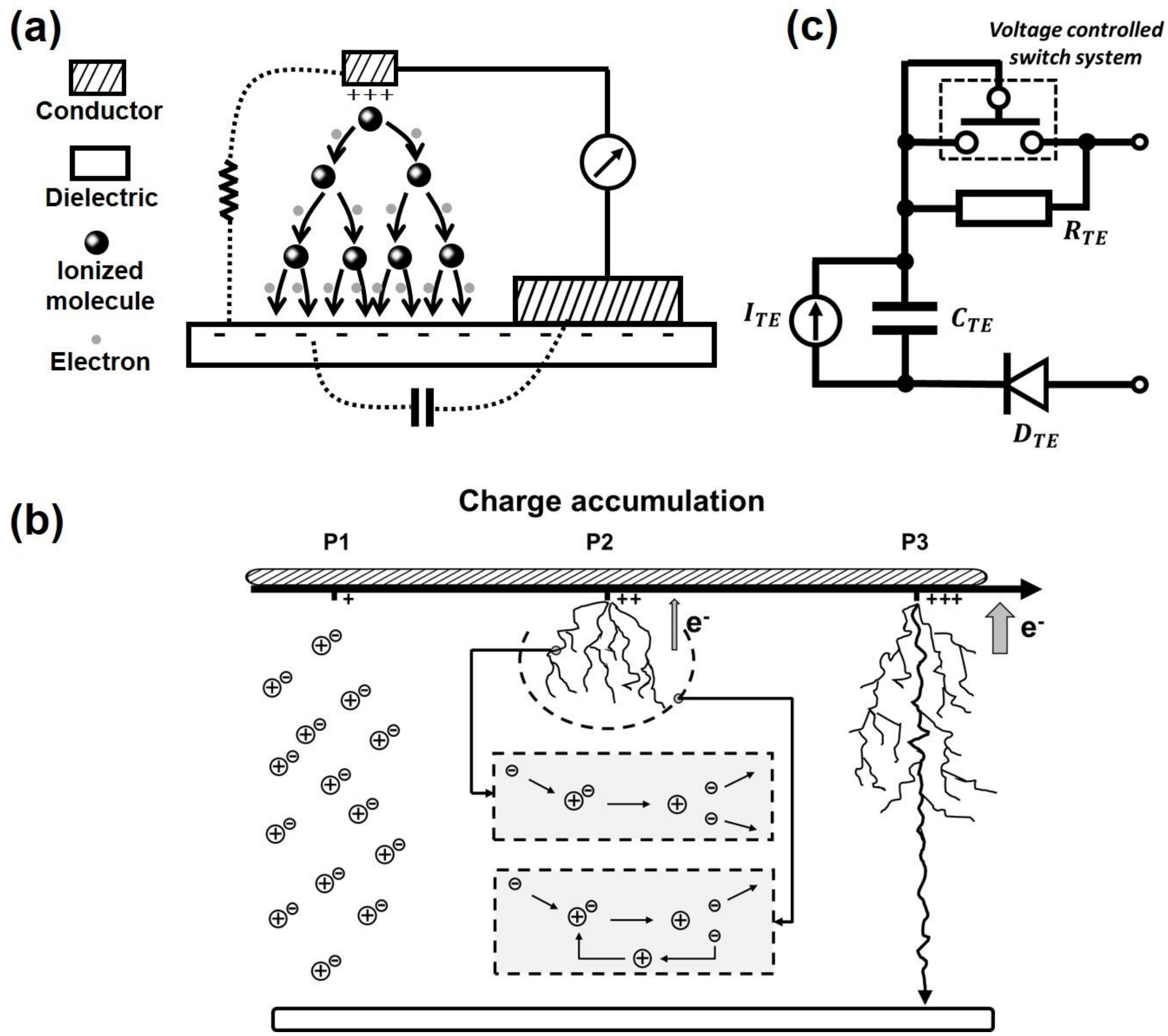
(a)
Conductor
Dielectric
Ionized molecule
Electron
+++
(c)
Voltage controlled switch system
R_{TE}
I_{TE}
C_{TE}
D_{TE}
(b)
Charge accumulation
P1
P2
P3
+
++
+++
e-

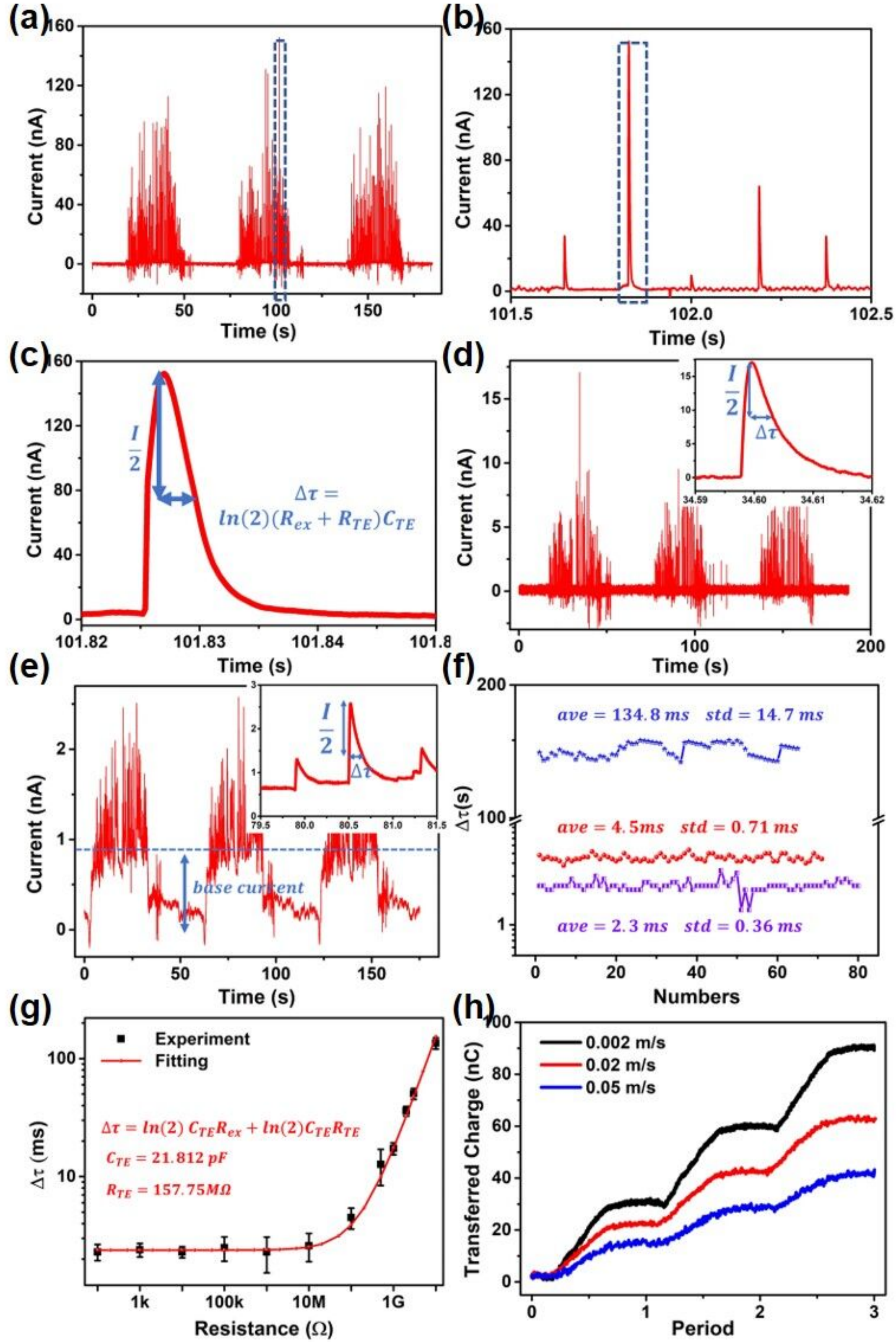
(a)
Current (nA)
Time (s)
(b)
Current (nA)
Time (s)
(c)
Current (nA)
Time (s)
I/2
$\Delta\tau = ln(2)(R_{ex} + R_{TE})C_{TE}$
(d)
Current (nA)
Time (s)
I/2
Δτ
(e)
Current (nA)
Time (s)
I/2
Δτ
base current
(f)
Δτ(s)
Numbers
$ave = 134.8\ ms \quad std = 14.7\ ms$
$ave = 4.5ms \quad std = 0.71\ ms$
$ave = 2.3\ ms \quad std = 0.36\ ms$
(g)
Experiment
Fitting
$\Delta\tau = ln(2)\ C_{TE}R_{ex} + ln(2)C_{TE}R_{TE}$
$C_{TE} = 21.812\ pF$
$R_{TE} = 157.75M\Omega$
Δτ (ms)
Resistance (Ω)
(h)
0.002 m/s
0.02 m/s
0.05 m/s
Transferred Charge (nC)
Period

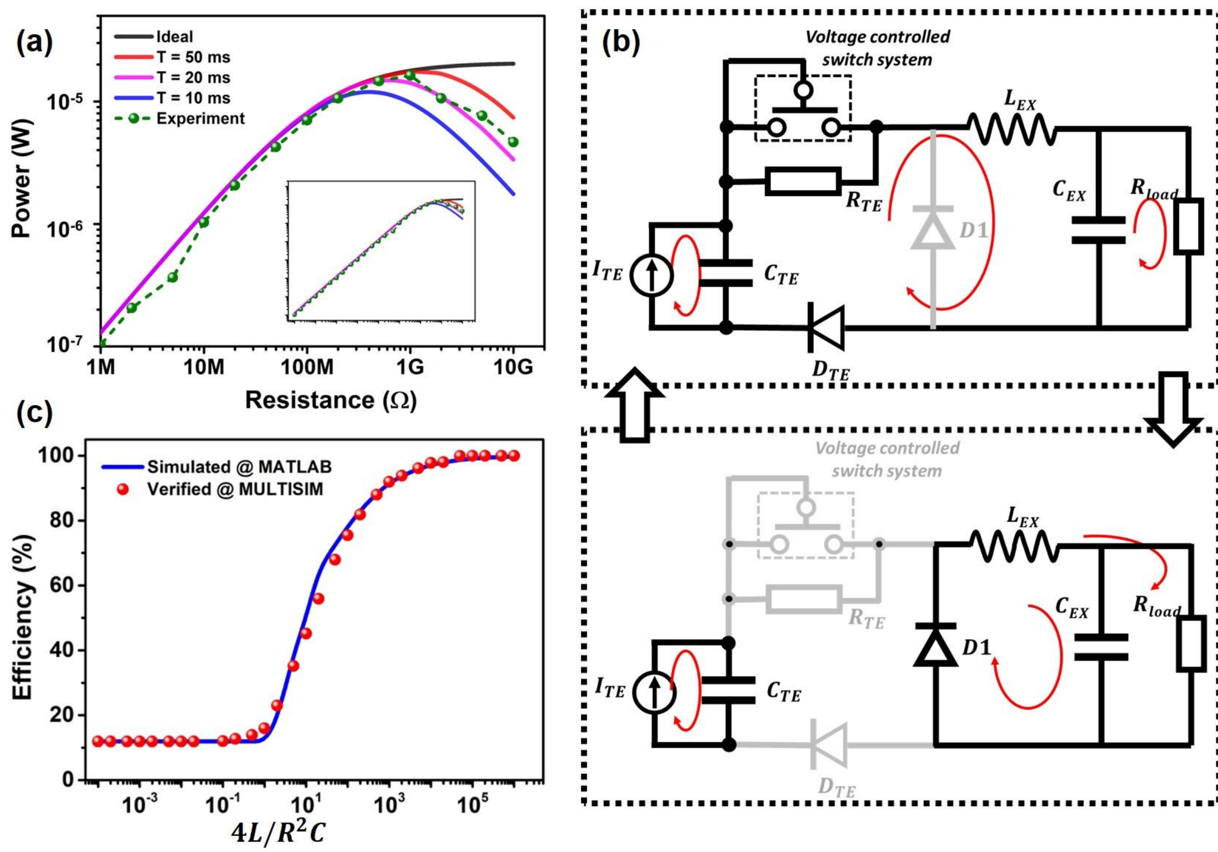
(a)
Ideal
T = 50 ms
T = 20 ms
T = 10 ms
Experiment
Power (W)
Resistance (Ω)
1M
10M
100M
1G
10G
(b)
Voltage controlled switch system
L_{EX}
R_{TE}
C_{EX}
R_{load}
$D1$
I_{TE}
C_{TE}
D_{TE}
(c)
Simulated @ MATLAB
Verified @ MULTISIM
Efficiency (%)
$4L/R^2C$